Phase Selection and Microstructure Evolution in Laser Additive Manufactured Ni-Based Hardfacing Alloy Bush

S. HARIBABU, C. SUDHA, C.P. PAUL, V. SRIHARI, ALPHY GEORGE, A. DASGUPTA, and K.S. BINDRA

Nickel-based hardfacing alloy bushes are used in dynamic moving components inside fast breeder reactors. Due to the difficulties associated with their fabrication through casting or weld deposition, laser rapid manufacturing (LRM) was attempted. In this work, microstructure development and phase selection in laser additive manufactured Ni-based hardfacing alloy bushes are investigated. The as-fabricated bushes had a uniform, defect-free microstructure perpendicular to the material build direction, whereas microstructural heterogeneity could be detected parallel to the build direction due to coarsening of precipitates. Overall microstructure was dominated by γ-Ni, γ-Ni + Ni$_3$B anomalous and lamellar eutectic and Ni–B–Si lamellar eutectic constituents. In addition, Cr-rich borides and carbides were also found. Phase property diagrams and Scheil's non-equilibrium solidification simulated using ThermoCalc® provided supporting insights into the phase selection phenomena under rapid cooling conditions. Microstructure of LRM Ni-based hardfacing alloy bushes was quite distinct from weld deposited ones and is analyzed in terms of a non-equilibrium eutectic solidification reaction occurring in Ni–Cr–B–C–Si–Fe multicomponent alloy system due to rapid cooling.

I. INTRODUCTION

HIGH-TEMPERATURE wear-resistant hard facing alloy bushes are required in dynamic moving components of control and diverse safety rod drive mechanisms, primary and secondary sodium pumps, and transfer arm gripper assembly in fast breeder reactors (FBRs).[1,2] Due to the challenges caused by induced activity of Stellite®, a widely used Co-based alloy, Ni-based hardfacing alloys are chosen as alternate structural materials for the bushes.[1,2] Nickel-based self-fluxing hard facing alloys that contain Cr, B, Si, and C provide excellent wear resistance and high-temperature oxidation resistance due to their higher Cr content and the presence of hard borides and carbides.[3,4]

NiCrBSi alloys with microstructure dominated by low-temperature eutectics such as Ni$_3$B and Ni$_3$Si were primarily developed for high-velocity oxy fuel thermal spray coatings.[5] Microstructure of these alloys is dictated by the deposition process and alloy chemistry. For example, in laser cladding, laser power, beam diameter, powder feed rate, translational speed of the beam, type of substrate, or the cooling rate can be changed to obtain deposits of varying microstructure, phase stability, and properties.[6–8] In alloys with the same composition, the morphology, type, and distribution of phases and the resultant properties could be changed just by altering the deposition technique and its parameters.[9–1] NiCrBSiC alloys of same composition deposited through laser cladding and flame spraying showed variation in the type of carbides, primary borides, equilibrium, and non-equilibrium eutectics.[12,13] Much finer and reduced volume fraction of precipitates could be obtained by increasing the cooling rate through replacement of the build plate.[14,15] It is seen from such studies that higher alloy grades (high Cr but low Si/B ratio) are more sensitive to the cooling rates due to their unique solidification paths.[16,17] In multilayer deposits, heat energy imparted by the incident beam, multiple thermal cycles undergone by the layers during deposition, and the rate of extraction of thermal energy across the entire cross section of the

S. HARIBABU and ALPHY GEORGE are with the Metallurgy and Materials Group, IGCAR, Kalpakkam, Tamilnadu 603102, India. Contact e-mail: haribabu.mme@gmail.com C. SUDHA and A. DASGUPTA are with the Metallurgy and Materials Group, IGCAR and also with the Homi Bhabha National Institute, Anushakthi Nagar, Mumbai 400085, India. C.P. PAUL and K.S. BINDRA are with the Laser Technology Division, RRCAT, Indore 452013, India and also with the Homi Bhabha National Institute. V. SRIHARI is with the High Pressure and Synchrotron Radiation Physics Division, BARC, Mumbai 400085, India.

deposit should be considered while interpreting the microstructure.[9]

Correlation of microstructure and microchemistry of the hardfacing deposit with properties is extremely important as the type of phases present, their size, shape, distribution, and crystallographic orientation, along with their interaction with the matrix phase govern the mechanical, corrosion, and wear properties.[18] Yet, there are very few studies[9,12,16,17,19,20] that are tuned toward this objective and some of the salient findings are with the increase in the concentration of C, B, Si, or Cr, volume fraction of soft primary dendrites decreased and that of hard borides and carbides increased.[12,17] Chromium in excess of 10 wt pct promoted the formation of borides as the primary phase and in alloys containing Cr, B, and C, there is competition between the formation of borides and carbides.[19] With the increase in Fe and Si contents, Cr had a tendency to segregate to interdendritic regions to form hard phases and the type of eutectic formation was decided primarily by Si/B ratio.[16] Apart from these studies, majority of the literature is on the effect of dilution on the structure and properties of the deposit.[21–26] Dilution leads to reduction in the volume fraction of hard phases resulting in graded microstructure.[25,27,28] In a gas tungsten arc welded Colmonoy 6® on SS, the desired properties could be achieved only after a distance of 2 to 2.5 mm from the interface due to the dilution effect.[21–23] Effect of dilution was more prominent on the size, morphology, volume fraction, and distribution of borides than carbides.[26]

To fabricate defect-free hardfacing alloy bushes for FBR application, an appropriate process with minimum dilution had to be identified. An indirect welding route was tried to avoid the difficulties faced in sourcing the as-cast bushes.[29] It required precise control of process parameters and several post-machining steps, resulting in huge material loss. In addition, dilution of the deposit by the substrate adversely affected the properties and lead to a higher threshold for the minimum thickness required for the deposit.[22,23] To overcome these difficulties, a novel 3D printing technique namely laser rapid manufacturing (LRM) or direct energy deposition by laser beam was adopted for manufacturing the bushes.[30]

The present study deals with characterization of the microstructure and phase stability of Ni-based hardfacing alloy bushes fabricated through LRM. Microstructural features of the additively manufactured bushes have been investigated using optical, scanning and transmission electron microscope, electron microprobe, and synchrotron XRD. Supporting evidences for segregation and phase selection are obtained from Scheil's non-equilibrium and phase property diagrams simulated using ThermoCalc®. Effect of compositional changes on the type of phases has been quantitatively established using ThermoCalc®. The observed microstructure is understood based on non-equilibrium eutectic solidification reaction occurring in Ni–Cr–B–C–Si–Fe multicomponent alloy system. Results are compared with literature information on the bushes fabricated through the welding route and finally possible effects on the properties are discussed.

II. EXPERIMENTS

Chemical composition of Ni-based hardfacing alloy feed powder used for the fabrication of bushes, as obtained using inductively coupled plasma optical emission spectroscopy (ICP-OES) is given in Table I. The feed powder particles were spherical in shape with a diameter in the range of 40 to 180 μm with maximum number of particles having a size of ~ 100 μm.

The LRM machine consisted of 10 kW CO_2 laser integrated with beam delivery system, co-axial powder feeder, and a 3-axis sample manipulation station, further details of which are given elsewhere.[30] During deposition, Ar was used as both shielding and carrier gas. Initial parametric studies for LRM were carried out in single and multitrack specimen with the aim of eliminating the cracks and other defects. Based on these experiments, the optimized parameters (Table II) were chosen and the bushes fabricated with the optimized parameters alone were taken up for a detailed metallographic characterization. To avoid cracking, deposition was done layer by layer on a preheated (at 673 K) SS 304L substrate. After fabrication, the specimens were buried in a sand bath for roughly 8 hours to achieve slow cooling. Then machining was carried out in sequential steps using specialized high-speed steel (with 10 pct Co) tool, Cermet inserts, and aluminum oxide grinding wheel to achieve the required dimensional tolerances and surface roughness. The Ni-based hardfacing alloy bush fabricated through LRM had length and wall thickness of 20.2 and 1.5 mm, respectively. The required dimensional tolerance after fabrication and machining was $\pm$ 0.1 mm with minimum 95 pct of theoretical density (8.14 g/cm^3), minimum hardness of 595 HV, and surface finish of 0.8 μm. Figures 1(a) and (b) are the photographs of as-deposited and final machined bushes that met all the design requirements. The room temperature density of the bushes measured by water immersion method using Sartorius® physical balance was 7.971 $\pm$ 0.008 g/cm^3, which is 97.9 pct of theoretical density.

From the fabricated bushes, smaller specimens were extracted, ground, polished, and etched following standard metallographic procedures. To study the microstructure of this multiphase material, specific etchants had to be used. While Murakami reagent [10 g $K_3Fe(CN)_6$ + 10 g NaOH + 100 mL H_2O] could reveal γ-Ni, chromium-rich carbides and borides, eutectic structures could be seen clearly only after etching the specimen with a solution of 5 mL HCl + 3 mL HNO_3 in 5 mL H_2O. For examination of the microstructure along (longitudinal) and perpendicular (transverse) to the build direction, optical (Zeiss Axio Observer) and scanning electron microscopes (SEM; FEI Helios Nanolab 600i) were used. SEM was operated at an accelerating voltage and current of 30 kV and 2.7 nA, respectively. Micrographs obtained in the backscattered electron (BSE) imaging mode made it easier to identify various phases from atomic number (Z) contrast. Hardness was measured with Leitz microhardness tester at an applied load of 100 g with a dwell time of 15 seconds. Minimum of 10 measurements were taken from similar locations to arrive at an average hardness value.

Synchrotron XRD experiments were carried out using angle dispersive X-ray beamline (BL-11) at Indian Synchrotron Source-2, RRCAT Indore. A monochromatic 17 keV X-ray beam and image plate detector setup was utilized to measure diffraction in reflection mode. The NIST LaB$_6$ powder was used for calibration of the wavelength, and the image plate data were converted to intensity *vs*. 2θ data using FIT2D software. Confirmatory evidence for the presence of various phases was obtained comparing the 2θ and peak intensity values with standard ICDD databases.[31]

Microchemical analysis was carried out using Cameca SX-Five Electron Probe Micro-Analyzer (EPMA) or electron microprobe attached with three wavelength-dispersive spectrometers (WDS) at an accelerating voltage of 20 kV and stabilized beam current of 20 nA. Elemental redistribution among various phases was identified through a combination of X-ray mapping,

point and line mode of analysis. X-ray mapping was done in the stage stepping mode with a step size of 0.4 μm with a dwell time of 15 seconds. Line scan was performed in the beam scanning mode with a step size of 0.1 μm and dwell time of 5 seconds. Diffracting crystals used in WDS were LiF for Ni Kα and Cr Kα, TAP for Si Kα, and PC2 for B Kα and C Kα. In quantitative analysis, the X-ray intensities obtained were compared with standards and corrected for atomic number, absorption, and fluorescence effects to get accurate concentrations. Electron transparent thin foil specimens were prepared from the bushes through jet thinning using 9:1 volume mixture of ethanol and perchloric acid at 238 K at 20.5 V. They were examined at 200 kV using Philips CM200 transmission electron microscope (TEM) fitted with energy-dispersive spectrometer (EDS).

To understand the formation of complex microstructures in the multiphase deposit, isopleths and phase property diagrams were simulated using the TCNI8 database in ThermoCalc®. All the phases reported to form in Ni-based hardfacing alloys such as γ-Ni, Ni$_3$B, Cr$_5$B$_3$, Cr$_3$C$_2$, CrB, Cr$_2$B, Cr$_7$C$_3$, Ni$_3$Si, Ni$_5$Si$_2$, Cr$_5$Si$_3$, and Cr$_{23}$C$_6$ were included in the calculation. Further, solidification sequence of phases was critically compared between Scheil non-equilibrium and ThermoCalc® equilibrium calculations.

Table I. Chemical Composition of Ni-Based Hardfacing Alloy Powder Used in the Present Study

Concentration of the Elements (in Wt Pct)					
Cr	Si	Fe	C	B	Ni
13.25	4.0	4.0	0.5	2.3	bal.

Table II. Process Parameters Used During LRM

Parameter	Value
Laser Power	2.5 kW
Scan Speed	4.2 mm/s
Powder Feed Rate	4 g/min
Track to Track Overlap in xy Plane	60 pct
Height Between Successive Layers	0.4 mm
Laser Spot Diameter	3 mm
Gas Shielding	Argon
Ar Gas Flow Rate	10 slpm

III. RESULTS

To infer the changes in the microstructure of additive manufactured hardfacing alloy bushes, investigations were carried out both in the longitudinal (along the build) and transverse (perpendicular to the build) directions.

A. *Microstructure of LRM Bushes*

1. *Transverse direction*

Optical micrograph obtained from the transverse section of the bushes is shown in Figure 2(a). Uniform and fine dendritic solidification structure was observed
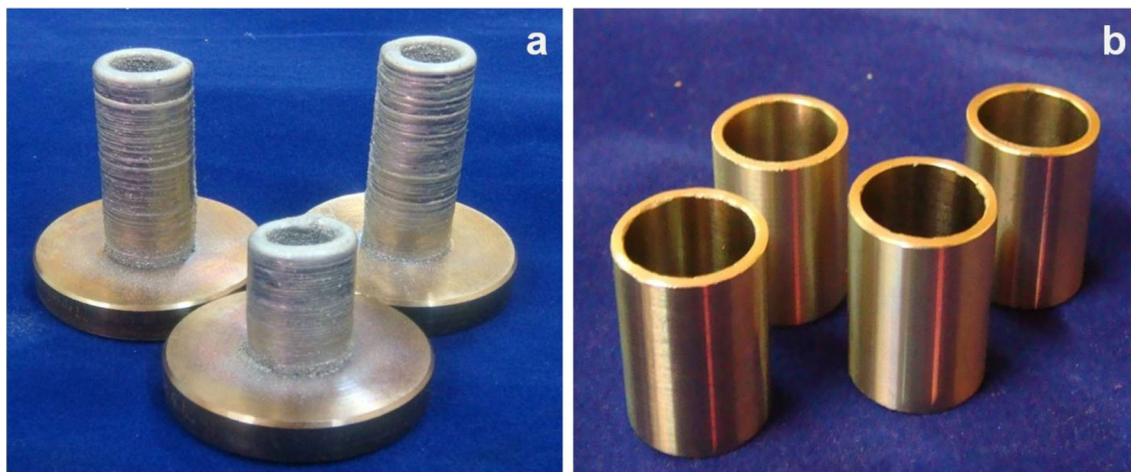

Fig. 1—Photograph of (*a*) as-deposited and (*b*) machined Ni-based hardfacing alloy bushes.

perpendicular to the build direction. Spherical- and irregular-shaped dark features (circled in Figure 2(a)) that appeared like porosity in the interdendritic regions need further investigation. Secondary electron (SE) image (Figure 2(b)) indicated the presence of various phases in the transverse direction that are labeled based on the observed contrast and morphology. There are anomalous eutectic solidification structures (labeled as A, B, and C in Figure 2(b)), lamellar eutectics (D), sparingly appearing few micron-sized gray phase (E), low volume fraction of dark phase (F) in the interdendritic region, and extremely fine, spherical gray features (G) appearing inside 'B.'

2. Longitudinal direction

Optical micrograph obtained from the longitudinal section of the bushes is shown in Figure 3(a). A layered structure was observed across the length of the bush due to layer-by-layer deposition of the material during LRM. Hence, during the process, overlapping of the layers can also be expected. Examination of the microstructure at high magnification (Figure 3(b)) revealed a fine dendritic solidification structure within the layers. In the layer overlap region (LOR; indicated by dotted line in Figure 3(b)), coarsened dendrites could be seen with a relatively low hardness of 625 HV0.1 compared to those within the layers (740 HV0.1). In addition, from the BSE image (Figure 3(c)), higher volume fraction (V_f) of precipitates (0.027) was observed in LOR compared to layer interiors (V_f = 0.021). The precipitates were coarsened in LOR with ~ 25 pct with size < 1 μm^2 compared to ~ 40 pct in layer interiors. As shown in Figure 3(d), the A and B phases had both irregular and lamellar morphology. At a higher magnification, the structure (Figure 4) was similar to that observed in the transverse direction (Figure 2(b)). The feature identified as 'E' was clearly visible when the specimen was etched with Murakami's reagent and the resultant BSE image is shown as an inset in Figure 4 ('E' is indicated by arrows).

B. Identification of Phases Present in LRM Bushes

1. Regions A, B, and C

In the as-deposited bushes, the presence of various phases such as γ-Ni, Ni_3B, Ni_3Si, CrB, Cr_5B_3, Cr_3C_2, Cr_7C_3, $Cr_{23}C_6$, and Cr_5Si_3 could be confirmed through diffraction analysis using Synchrotron radiation (Figure 5). Though many of the diffraction peaks are common to multiple phases, it was possible to identify individual signature peaks for each confirmed phase due to high sensitivity of synchrotron XRD. The next step was to explore the size, distribution, and morphology of these phases in the as-deposited bushes. Phases labeled as A and B in Figures 2(b) and 4 are both rich in Ni, 'A' getting preferentially etched indicating difference in chemistry. From XRD pattern (Figure 5) possibility of existence of only two Ni-rich phases is seen, i.e., FCC γ-Ni solid solution and orthorhombic Ni_3B. EPMA analysis confirmed the enrichment of boron in phase 'B' (76.63Ni–5.23Cr–3.25C–0.39Si–1.4Fe–13.1B, wt pct) compared to phase 'A' (82.42Ni–7.16Cr–2.72C–4.7-Si–3Fe, wt pct). Figures 6(a) and (b) show the Bright-Field (BF) image and Selected Area Diffraction (SAD) pattern obtained using TEM from phase 'B'. Analysis of the SAD pattern confirmed phase 'B' to be Ni_3B. Submicron-sized dark phases in the interdendritic regions ('C' in Figures 2(b) and 4) could not be analyzed using either SEM/EDS or electron microprobe. Analysis of the SAD pattern obtained from thin foil specimens using TEM (Figures 6(c) and (d)) confirmed the presence of Cr_3C_2-type carbides. An interesting observation was the presence of cuboidal particles within secondary γ-Ni dendrites (Figure 7(a)) in the as-deposited bushes. EDS spectrum (Figure 7(b)) showed enhancement in both Ni and Si concentration in these particles. Combining this information with XRD data it is concluded that the particles are Ni_3Si-type nickel silicides.

2. Region D

Lamellar eutectics of different morphologies (labeled as D in Figures 2(b) and 4) were found in few interdendritic regions. Similar structures have been
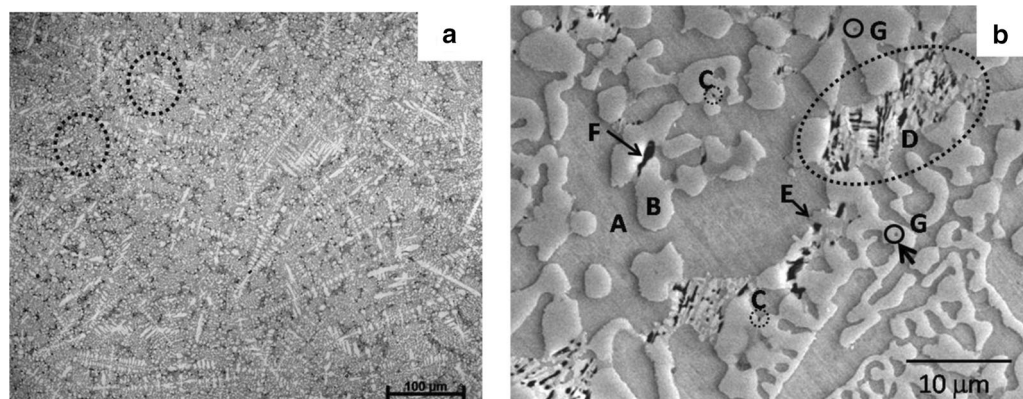

Fig. 2—(a) Optical micrograph and (b) SE image obtained from the transverse section of LRM Ni-based hardfacing alloy bush; phases are labeled in (b) based on observed contrast and morphology.
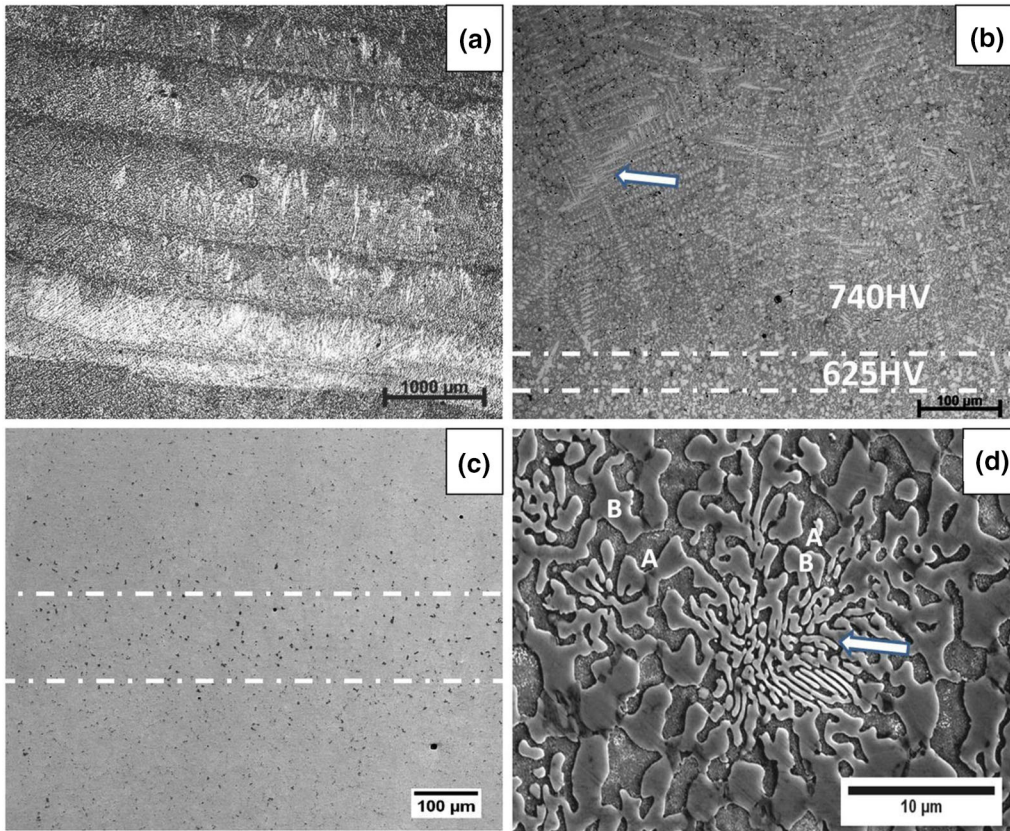
Fig. 3—Optical micrograph obtained along longitudinal direction showing (*a*) several layers of the deposit, (*b*) dendritic solidification mode inside the layers (shown using arrow) and difference in microstructure and hardness between layer overlap region (LOR shown as dotted lines) and inside the layers, (*c*) BSE image showing relatively high volume fraction of phases having dark contrast in LOR (indicated by dotted lines), and (*d*) SE image showing both irregular and lamellar (indicated by arrow) morphology of A and B phases.
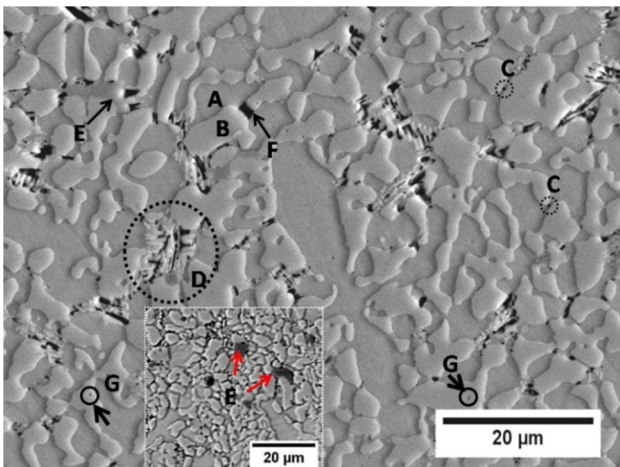
Fig. 4—BSE image obtained from the longitudinal section of LRM bushes showing the presence of various phases (labeled); inset shows the BSE image after etching the specimen with Murakami's reagent clearly revealing the phase labeled as 'E'.

Fig. 5—Synchrotron XRD pattern obtained from LRM Ni-based hardfacing alloy bush.

observed earlier in NiCrSiCB alloys due to preferential segregation of elements at terminal stages of solidification.[17,18] BSE image and X-ray maps for Si, C, and B obtained from one such region are given as Figures 8(a) through (d), respectively. X-ray maps showed the

enrichment of Si (Figure 8(b)) in the dark regions (indicated by solid white arrows in Figure 8(a)) that form a part of the lamellar structure. The bright and gray regions in the lamellar structure are both Ni-rich with boron enrichment in the bright region, implying the
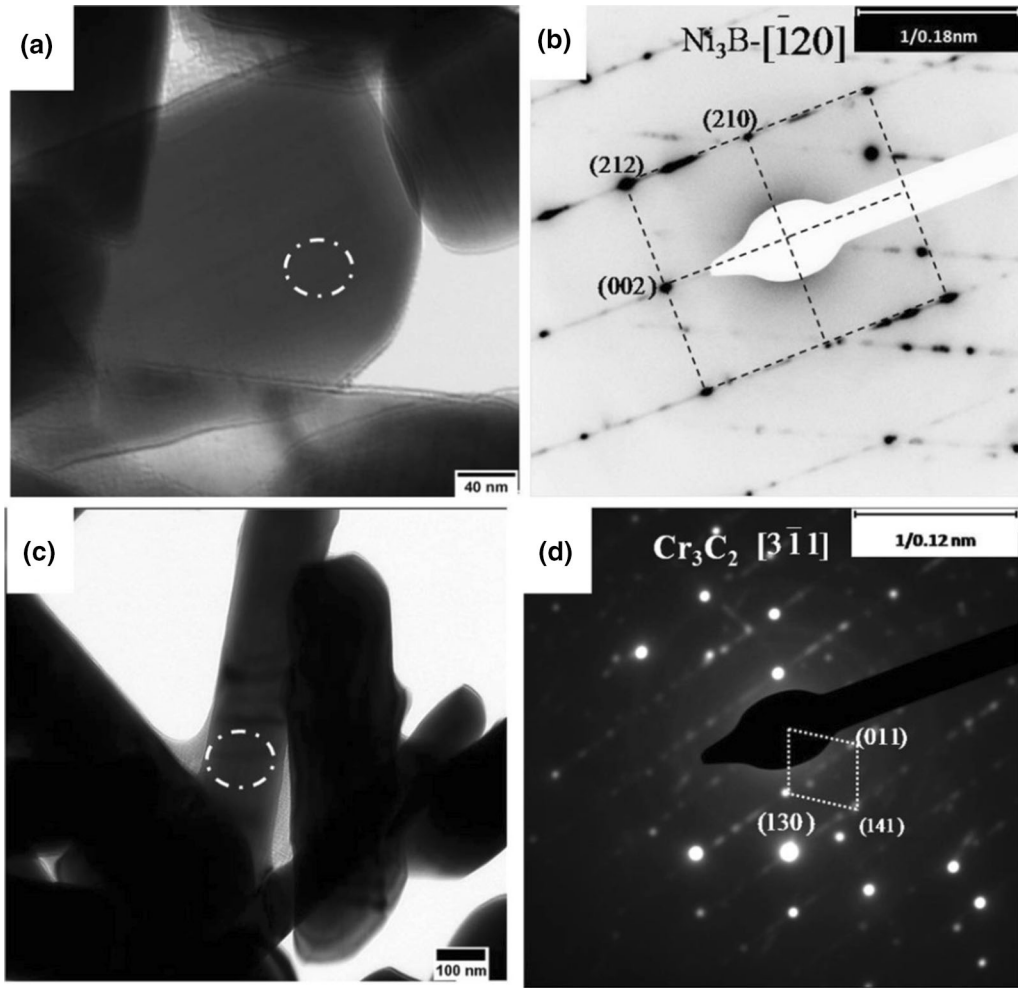
Fig. 6—TEM bright-field micrographs and corresponding SAD patterns with zone axis for (*a, b*) Ni$_3$B and (*c, d*) Cr$_3$C$_2$.
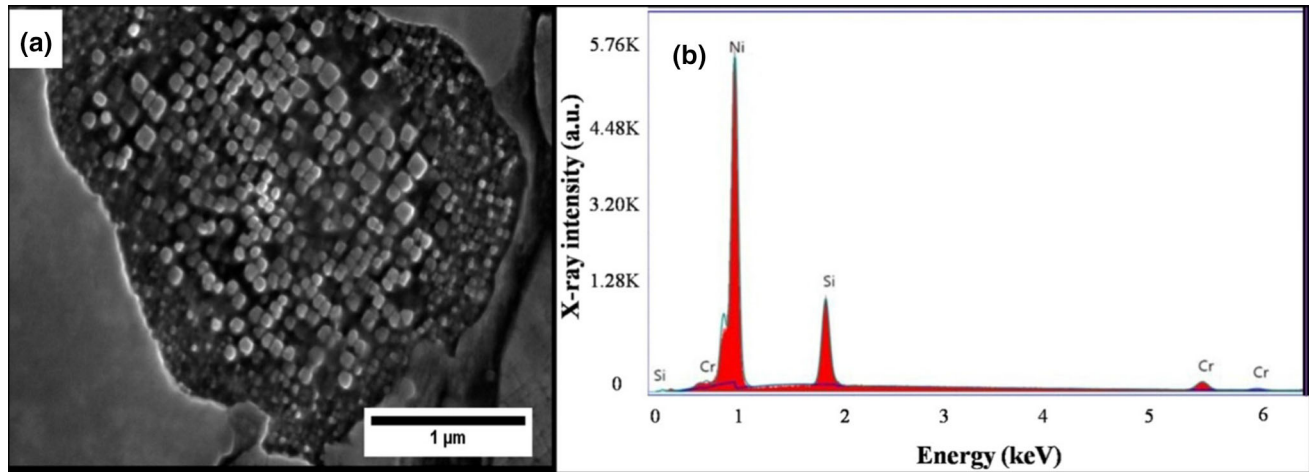

Fig. 7—(*a*) SE image and (*b*) EDS spectrum showing Ni and Si enrichment in the cuboidal particles inside secondary γ-Ni dendrites.

lamellar structures to be Ni–B–Si eutectics. In addition, X-ray map (Figure 8(c)) also showed the presence of ~ 2 to 2.5 μm sized carbides (shown using dotted arrow in Figure 8(a)) in the interdendritic regions.

3. Region E and F

The dark features labeled as 'E' and 'F' in Figure 2(b) are coarser in the LOR, hence further analysis was carried out in this region. Phase 'E' was clearly visible
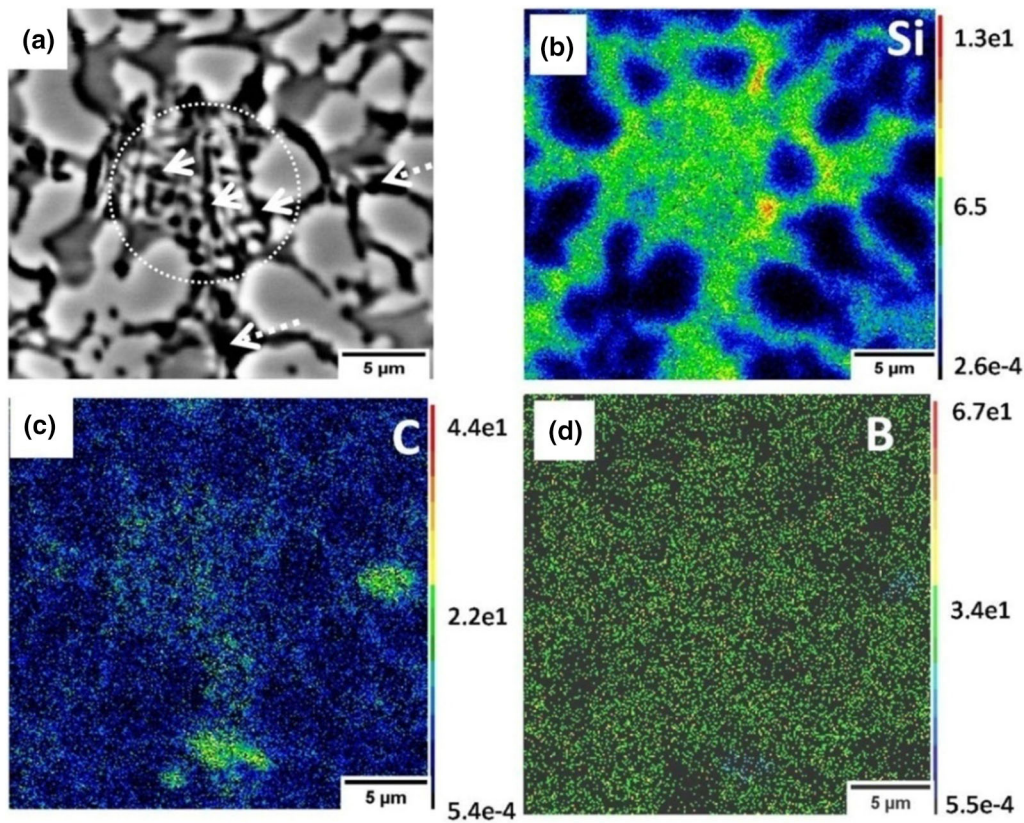
Fig. 8—(*a*) BSE image; X-ray maps for (*b*) Si, (*c*) C, and (*d*) B obtained from the region shown in (a) (Color figure online).

when the specimen was etched with Murakami's reagent. Figures 9(a) through (f) are the BSE image and X-ray maps for Ni, Cr, C, Si, and B, respectively, obtained from the LOR. Since predominant phase in the structure was γ-Ni + Ni$_3$B good contrast could not be obtained for boron. From the BSE image (Figure 9(a)) and X-ray maps (Figures 9(c) and (d)), the features E and F were found to be Cr-rich carbides. The interdendritic regions corresponding to lamellar Ni–B–Si eutectics showed enhancement in Si concentration (Figure 9(e)) as seen before. Using EPMA, average compositions in E and F regions were obtained as 17.77Ni–66.72Cr–11.63C–0.37Si–1.92Fe–1.59B, wt pct and 35.5Ni–49.72Cr–6.17C–4.10Si–2.22Fe–2.28B, wt pct, respectively. Among different carbides, carbon concentration (in wt pct) has the following order if 'M' is considered as Cr: Cr$_3$C$_2$ (13.3C, 86.7Cr) > Cr$_7$C$_3$ (9C, 91Cr) > Cr$_{23}$C$_6$ (6.6C, 93.4Cr). From EPMA analysis the bigger carbides (E) have ~ 11.6 pct ($\pm$ 1.7 pct) carbon, whereas the smaller ones (F) have ~ 6 pct ($\pm$ 1.6 pct) from which it is speculated that they are M$_7$C$_3$ and M$_{23}$C$_6$ carbides, respectively.

4. Region G

Out of all the phases confirmed to have formed in the bushes (Figure 5) morphology and nucleation sites for Cr borides and chromium silicides were difficult to identify. There were very fine precipitates (Figure 10(a)) appearing always inside the Ni$_3$B phase (labeled as G in Figure 2(b)) and it had enhanced Cr concentration

(Figure 10(b)). They could be Cr carbides, borides, or silicides. Since both Si and C were not detected in these fine precipitates they may be chromium borides (CrB or Cr$_5$B$_3$). Chromium silicides could not be identified in the microstructure probably because of their extremely fine size and low volume fraction.

C. Prediction of Phase Equilibria

1. Equilibrium conditions

As discussed in introduction, Ni–Cr–B–Si–C hardfacing alloy microstructures are highly sensitive to deposition process as well as chemistry due to variety of solidification paths that are possible. In the following section, an attempt has been made to understand the solidification path and resultant microstructure formation using ThermoCalc® calculations under equilibrium and non-equilibrium conditions.

In a detailed study of phase selection phenomena in laser deposited Ni–Cr–B–Si–C hardfacing alloy under different cooling conditions,[9] it was observed that the room temperature microstructure of the deposit consists of either blocky CrB or floret-shaped Cr$_5$B$_3$ as the primary boride. That is, the two structures are mutually exclusive due to unique solidification path followed by the alloy at different cooling rates. In this study, ThermoCalc® simulations were carried out to reflect the scenarios, where MB (CrB) or Cr$_5$B$_3$ formed as primary boride and also the preferred phase stability in the absence of these phases.
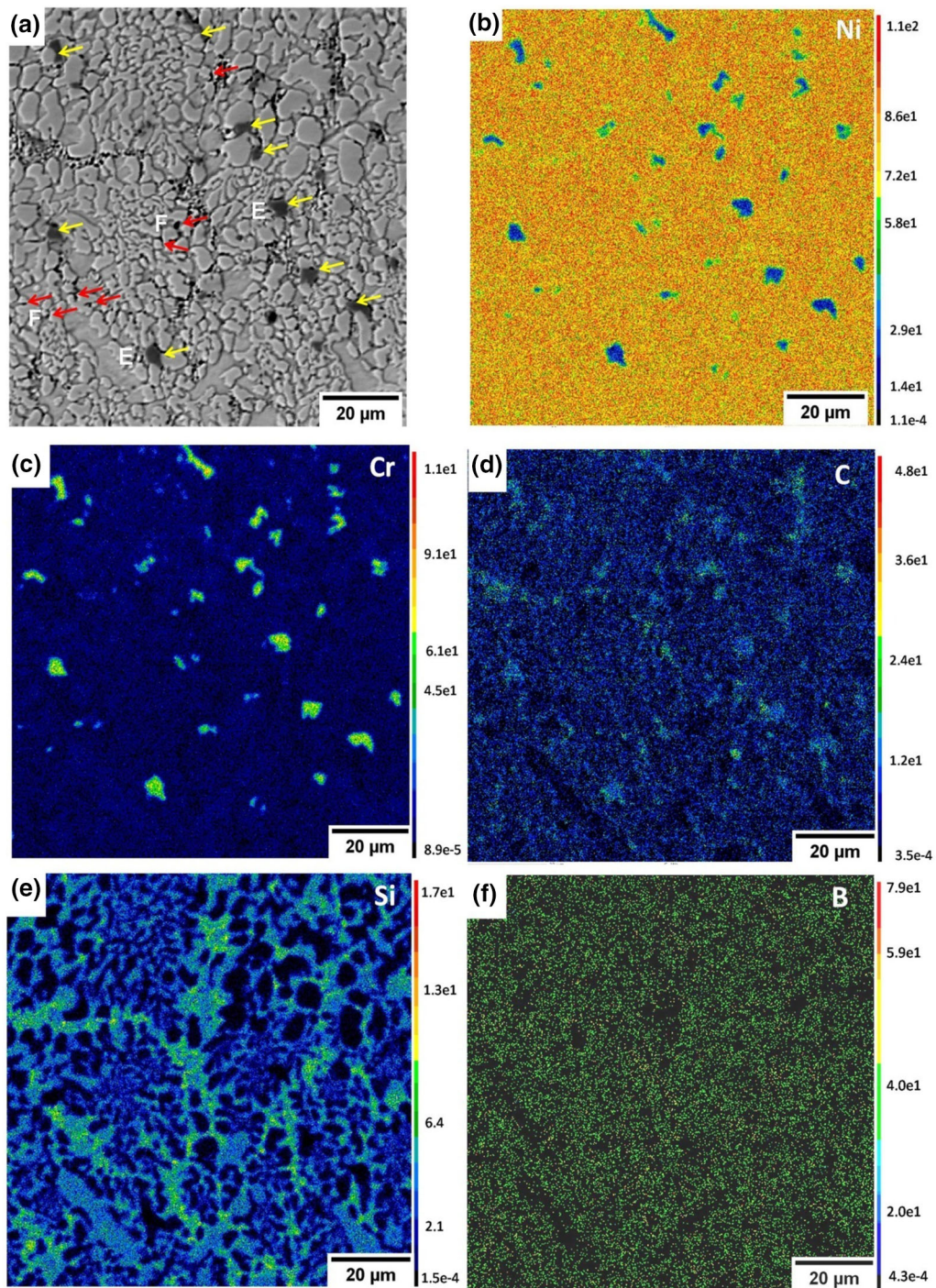
Fig. 9—(*a*) BSE image obtained from LOR after etching with Murakami's reagent showing two different dark phases labeled as E (indicated by yellow arrows) and F (indicated by red arrows) and corresponding X-ray maps for (*b*) Ni, (*c*) Cr, (*d*) C, (*e*) Si, and (*f*) B (Color figure online).

Figure 11(a) is the phase property diagram generated considering MB as the primary boride. Solidification starts with the precipitation of MB in the liquid phase followed by γ-Ni, MC, Ni_3B, and M_3C_2. Nature of carbide changes from non-stoichiometric MC (FCC phase rich in Cr and C) $\rightarrow M_3C_2 \rightarrow M_7C_3$ with increase in the concentration of Cr. As the solidification proceeds weight fraction (W_f) of both MB and γ-Ni increases and remains constant up to room temperature. Ni_3B phase starts forming at 1276 K (inset in Figure 11(a)), its W_f decreasing with temperature and dissolves completely at 733 K. For the given alloy composition, the room temperature microstructure is expected to have γ-Ni + high W_f (= 0.13) of coarsened MB + ≤ 0.01 W_f of M_3C_2. Nickel borides, silicides, and other types of chromium borides are not predicted to form at room temperature.
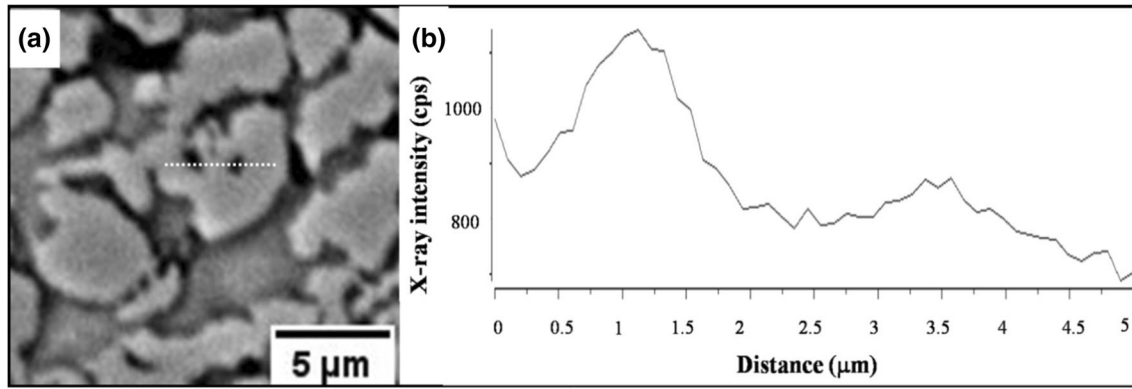
Fig. 10—(a) BSE image and (b) Cr intensity profile obtained across the dotted line in (a) showing Cr enhancement in the fine precipitates inside nickel boride.
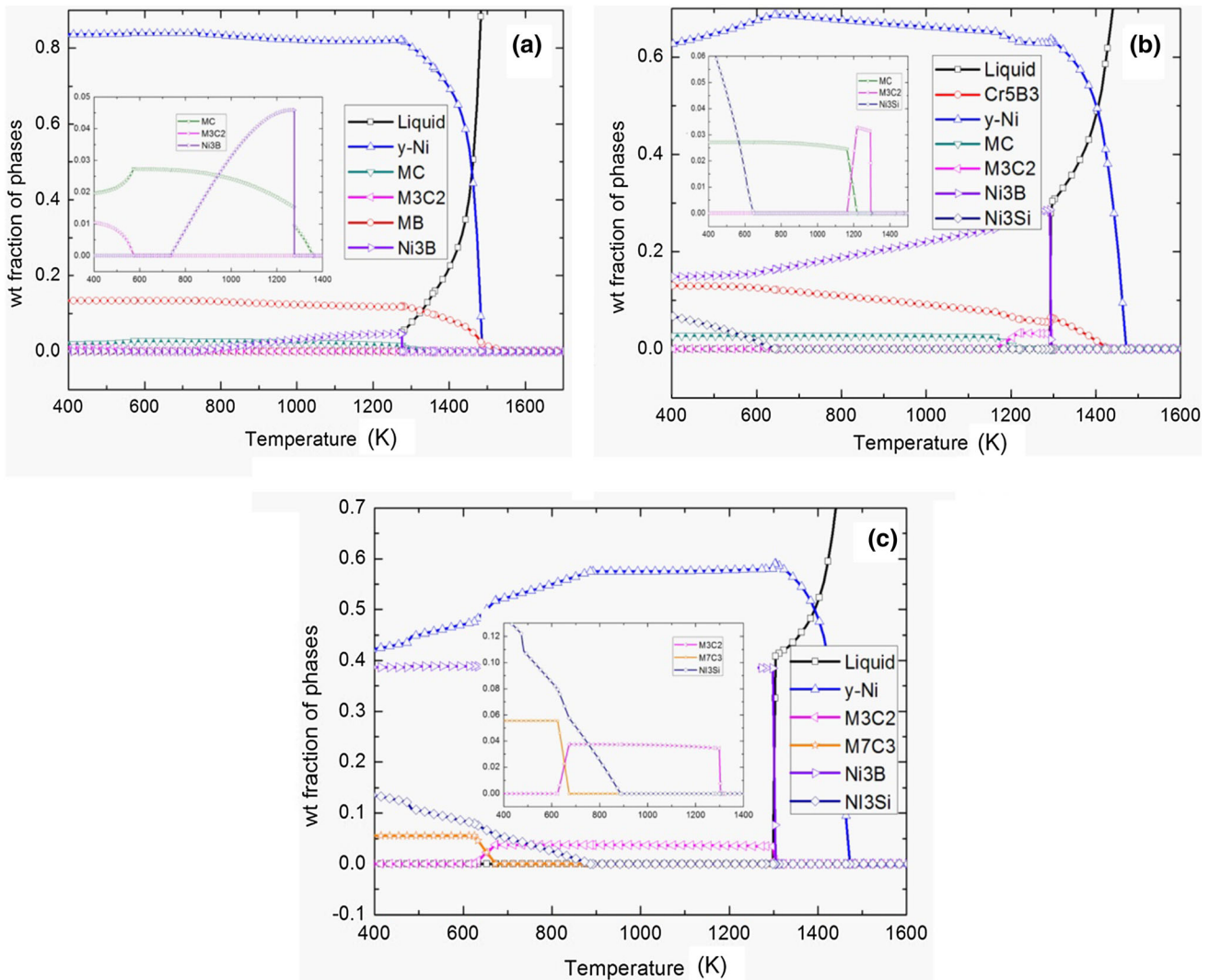

Fig. 11—Phase property diagrams for Ni-based hardfacing alloy when (a) MB is the primary boride, (b) Cr_5B_3 is the primary boride, and (c) primary Cr borides are absent. Insets show the precipitation and dissolution temperatures for minor phases.

When simulations were repeated with Cr_5B_3 as the primary boride (Figure 11(b)), it formed in the γ-Ni matrix phase starting from 1427 K followed by simultaneous precipitation of Ni_3B and M_3C_2 at 1293 K, hinting at a eutectic reaction involving γ-Ni, Ni_3B, and M_3C_2 phase. However, M_3C_2 was not

stable at temperatures < 1173 K and stability of Ni_3Si was restricted to lower temperatures (< 673 K). Phase constituents at room temperature are γ-Ni + Ni_3B + Cr_5B_3 + MC + Ni_3Si; W_f of Ni_3B always higher than Cr_5B_3.

When both Cr borides were not considered (Figure 11(c)) solidification started with γ-Ni, followed by eutectic γ-Ni + Ni_3B + M_3C_2 formation at 1298 K. Carbide stable at room temperature was M_7C_3 and stability of Ni_3Si was increased to 904 K. Equilibrium solidification simulations assuming complete equilibrium in both solid and liquid phases could bring out the effect of precipitation and dissolution of certain phases on the room temperature phase assemblage of the hardfacing alloy and also possible eutectic reactions in the system. However, in actual situations the most stable phases may not form due to kinetic reasons. Diffusion in the solid phase is very slow and hence if sufficient time is not given during cooling microsegregation effects can change the sequence of phase formation. Due to prevailing non-equilibrium conditions in LRM, Scheil solidification simulation gave better insights into the solidification process.

2. *Non-equilibrium conditions*

Classic Scheil simulation assumes complete mixing in the liquid phase and no diffusion in the solid phase, an assumption more valid for rapid solidification conditions where local composition changes dictate phase formation. Figures 12(a) through (c) are Scheil simulations considering MB or Cr_5B_3 as primary boride and after suspending the formation of these Cr borides, respectively. All the plots show variation in the W_f of phases as the solidification proceeds, represented by decrease in temperature. In Figures 12(a) and (b) first phase to form is similar to the equilibrium case (Figure 11). One striking difference in non-equilibrium simulation was the type of carbide that precipitated, *i.e.*, M_3C_2 rather than MC, which had highest fraction when both Cr borides were suspended (Figure 12(c)). In all the cases, eutectic γ-Ni + Ni_3B + M_3C_2 formed with the following differences in the room temperature microstructure: when MB or Cr_5B_3 was considered, Ni_3B precipitated as a proeutectic phase at 1286 K (Figure 12(a)) and 1306 K (Figure 12(b)), respectively, with eutectic transformation occurring at 1262 K (Figure 12(a)) and 1295 K (Figure 12(b)), respectively. When both borides were suspended (Figure 12(c)), the proeutectic phase was M_3C_2 that formed at 1319 K with eutectic formation at 1303 K. It is well known that primary boride phase has strong effect on subsequent formation of eutectics which is also well reflected in the present simulation.[26] With increased availability of boron in the matrix phase either due to the formation of Cr_5B_3 or complete elimination of the formation of chromium borides W_f of (Ni_3B, M_3C_2) in the eutectic increased from (0.15, 0.01) to (0.30, 0.022) and (0.34, 0.028), respectively. Ni_3Si was predicted to be stable only in the absence of chromium borides. Scheil's non-equilibrium solidification simulations predicted a ternary eutectic formation between γ-Ni, Ni_3B, and M_3C_2 carbides, in line with experimental observations

(Figures 2, 6, and 8). A consolidated list of all the phases predicted to form in the Ni-based hardfacing alloy under both equilibrium and a non-equilibrium solidification conditions is given as Table III.

IV. DISCUSSION

Based on the experimental observations, the LRM bushes are concluded to have the following microstructure and room temperature phase stability (Figure 13): predominantly γ-Ni + Ni_3B anomalous eutectic solidification structure with (a) low volume fraction of anomalous γ-Ni + Ni_3B + Cr_3C_2 ternary eutectics and precipitation of Ni_3Si inside γ-Ni secondary dendritic arms, (b) interdendritic lamellar γ-Ni + Ni_3B + Ni_3Si eutectics, (c) interdendritic $Cr_{23}C_6$ and Cr_7C_3 carbides, (d) extremely fine Cr borides inside few Ni_3B regions. Microstructure of the additive manufactured bushes is thus quite different from the weld deposited ones[29] that consist of bulky Cr borides and carbides in γ-Ni matrix.

The room temperature microstructure of the LRM bushes can be understood from an analysis of the unique solidification path followed by the alloy; taking clues from both simulations and experiment. In general, solidification starts with Cr borides/γ-Ni precipitation. Synchrotron XRD data (Figure 5) showed the presence of both CrB and Cr_5B_3 phases besides Ni_3B and Ni_3Si. According to ThermoCalc® simulations, precipitation of Cr borides will reduce the availability of boron in the matrix resulting in low volume fraction of Ni_3B and completely eliminating the formation of Ni_3Si, contrary to experimental observations. Equilibrium solidification simulations also do not predict the formation of Cr_3C_2 and $Cr_{23}C_6$ carbides present in the interdendritic regions of the bushes. Experimental observations are well matched with simulations when fast solidification-related effects such as high cooling rate and segregation are considered through Scheil calculation. Observation of Cr borides in addition to nickel borides and observation of Ni_3Si as a stable phase implies that Scheil non-equilibrium solidification simulation scenarios depicted in Figures 12(b) and (c) need to be combined to arrive at the room temperature microstructure.

A. *Formation of Cr Borides, Binary, and Ternary Eutectics*

The effect of cooling rate is maximum on the formation of borides than carbides.[16] Since both CrB and Cr_5B_3 are present (Figure 5), it is possible that the following reaction might have proceeded to some extent.

$$L + CrB \rightarrow Cr_5B_3.$$
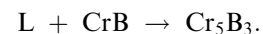
CrB if present would have formed directly from the liquid phase, whereas Cr5B3 precipitates in γ-Ni. The presence of low volume fraction of fine Cr borides inside Ni_3B (Figure 10) suggests extremely fast cooling rates which curtailed the precipitation and coarsening of these
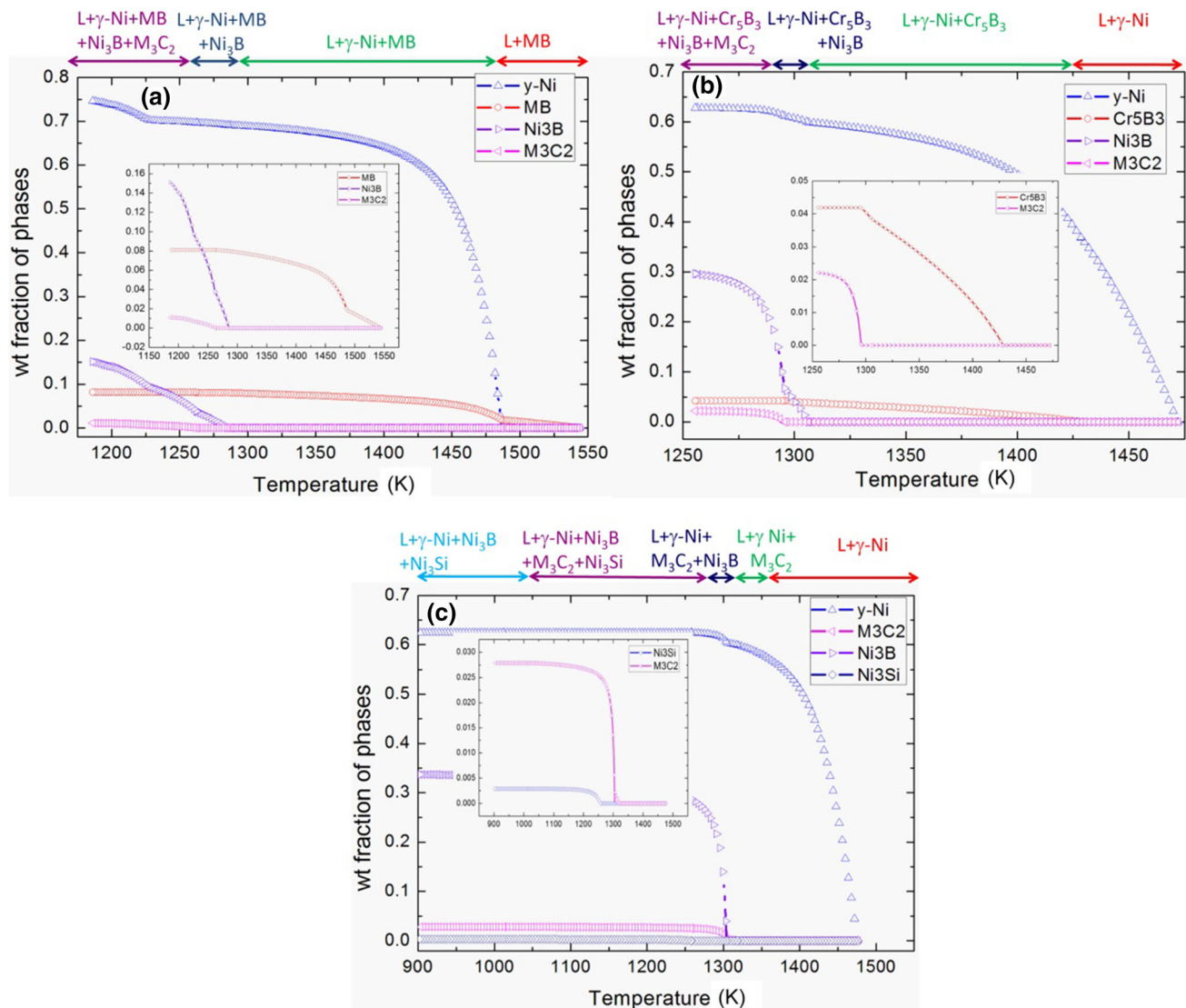
Fig. 12—Scheil simulation of the variation in weight fraction of phases with temperature when (*a*) MB or (*b*) Cr_5B_3 are considered as primary boride and (*c*) primary Cr borides are not considered as stable phases (labels on top of the diagrams indicate solidification sequence).

Table III. Consolidated List of Predicted Phases Under Equilibrium and Non-equilibrium Solidification Conditions

Solidification Condition	Assumptions Made During Simulation	Predicted Phases at Room Temperature (in Decreasing Order of W_f)
Equilibrium	primary boride—only MB	γ-Ni + MB + MC + M_3C_2
	primary boride—only Cr_5B_3	γ-Ni + Ni_3B + Cr_5B_3 + Ni_3Si + MC
	Cr borides—not considered	γ-Ni + Ni_3B + Ni_3Si + M_7C_3
Non-equilibrium	primary boride—only MB	γ-Ni + Ni_3B + MB + M_3C_2
	primary boride—only Cr_5B_3	γ-Ni + Ni_3B + Cr_5B_3 + M_3C_2
	Cr borides—not considered	γ-Ni + Ni_3B + M_3C_2 + Ni_3Si

borides. Accurate predictions of the volume fraction of Ni_3B phase (0.34) through Scheil simulation further supports this inference that the volume fraction of Cr borides if present will be extremely low. Since Cr_5B_3-type Cr borides increase the stability of nickel borides (Figure 12(b)) it is highly probable that most of

the Cr borides are of this type. Resultant higher availability of boron in the matrix phase combined with low solubility of boron in Ni (< 0.1 at. pct at 1123 K)[32] facilitates the formation of Ni3B. Hence, as the solidification takes place boron that segregates to the remaining liquid forms γ-Ni–Ni_3B eutectic structure.

These eutectics are present in various scales and morphologies as shown in Figure 3(d), dictated by the cooling rate. The presence of such anomalous and lamellar eutectics and existence of an orientation relationship between the participating phases has been reported earlier.[12,33–36] From Figure 11(b) it is clear that weight fraction of Cr_5B_3 reached saturation even before the precipitation of Ni_3B and it was not involved in the eutectic reaction. Sudden increase in the weight fractions of Ni_3B and M_3C_2 is an indication of a eutectic reaction between γ-Ni, Ni_3B and M_3C_2 phases according to Hillert's criteria.[37]

B. Formation of Cr Carbides

Previous studies have shown that solubility of C and Si in γ-Ni is low leading to the segregation of these elements to the interdendritic regions, similar to boron.[5,38] Iron and Si reduces the solubility of Cr in Ni.[5] It is possible to have differences in Cr concentration in localized regions due to non-equilibrium solidification thereby leading to the precipitation of Cr-rich carbides: $Cr_{23}C_6$, Cr_7C_3, and Cr_3C_2. These carbides are identified based on their relative size, composition, morphology, and nucleation site. As predicted by ThermoCalc®, Cr_3C_2 is the first carbide to form after primary γ-Ni dendrites and γ-Ni + Ni_3B anomalous eutectics. However, due to higher cooling rates sufficient time is not available for its growth and is therefore the finest of the three carbides, i.e., size of Cr_7C_3 > $Cr_{23}C_6$ > Cr_3C_2. While the relative carbon concentration of Cr_7C_3 and $Cr_{23}C_6$ could be compared, same could not be determined for Cr_3C_2 due to its extremely small size. Fine Cr_3C_2 carbides present always along with γ-Ni + Ni_3B anomalous eutectics could be identified from TEM–SAD analysis. As the solidification proceeds, though Cr_7C_3 carbides start precipitating the stability shifts to relatively Cr-rich $Cr_{23}C_6$, with reduction in the concentration of carbon. It is probable that the $Cr_{23}C_6$ carbides form during the terminal or last stage of solidification.
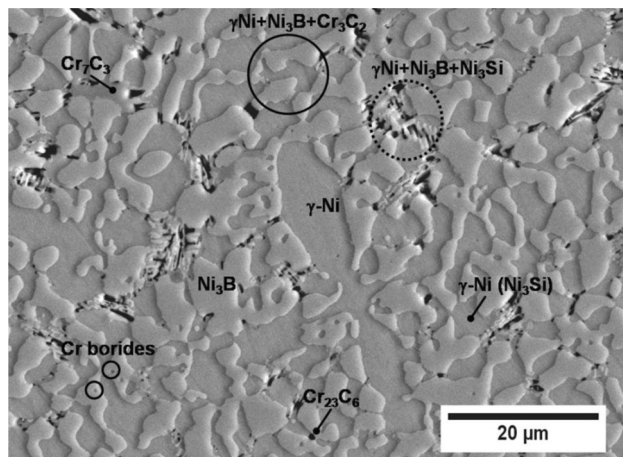
C. Formation of Lamellar Ni–B–Si Terminal Eutectics

Scheil simulation does not predict Ni–B–Si eutectic formation. However, it is possible that under actual conditions a combination of diffusion and mixing in the liquid state might have lead to higher Si segregation in the terminal liquid. These regions are the last to solidify to lamellar ternary eutectics as observed earlier in similar alloys.[14,17] Simulated composition profiles showed a complex interrelationship between the primary boride formation and composition evolution in γ-Ni dendrites. When Cr primary borides are absent, Si is predicted to segregate to γ-Ni and Cr and Fe to interdendritic regions (Figure 14). Thus, Si segregation is the main reason for the formation of nickel silicides (Figure 7) within γ-Ni dendrites, similar to the observation of Lebaili et al.[19] Differences in hardness and higher volume fraction of coarsened carbides in LOR compared to layer interiors may be due to thermal aging effects during layer-by-layer deposition.

In a previous study,[10] both laser and plasma clad Ni-based coatings had hypoeutectic structures. However, the laser clad layers had higher volume fraction of fine eutectic phases because of which the wear resistance was greatly improved. Similarly, Hemmati and E. E. Kornienko et al.[9,39] showed that the microstructures dominated by Ni–B–Si eutectics are harder than other structures with hard borides and carbides. Hardness of various borides and carbides reported to form in Ni-based hardfacing alloys are as follows[4]: CrB (2300 HV), Cr_3C_2 (1400 HV), Cr_7C_3 (1700 HV), Ni_3B (1000 HV), and Ni_3Si (600 HV). According to the composite model,[4] hardness of a composite can be obtained by combining the hardness of individual phases and their volume fractions. This means that deposits containing high volume fraction of relatively softer phases can have better properties than the ones having low volume fraction of harder phases. Thus, LRM bushes having fine eutectic solidification structure predominantly consisting of γ-Ni, Ni_3B, Cr_3C_2, and Ni_3Si binary and ternary eutectics are expected to have better wear properties compared to weld deposited ones.

Fig. 13—Typical microstructure and phase constituents of LRM Ni-based hardfacing alloy bush.

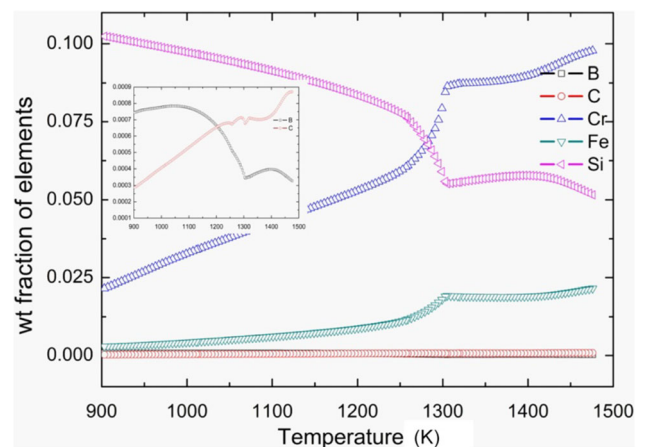
Fig. 14—Scheil simulation of composition variation in γ-Ni as a function of temperature in Ni-based hardfacing alloy when primary Cr borides are not considered.

V. CONCLUSIONS

Ni–Cr–B–C–Si–Fe hardfacing alloy bushes that are difficult to fabricate through conventional manufacturing processes could be successfully fabricated through laser rapid manufacturing, a 3D printing technique. The effect of solidification condition prevailing during 3D printing on the microstructure and phase stability of the alloy was investigated using both experimental techniques and simulation tools and the important conclusions from the study are as follows:

- LRM bushes had uniform microstructure in the transverse direction, whereas in the longitudinal direction microstructural heterogeneity was observed (coarsening of carbides) in the layer overlap region compared to layer interiors which resulted in slightly lower hardness.
- Microstructure of the bushes is dominated by γ-Ni + Ni$_3$B anomalous and lamellar eutectic constituents. In addition, low volume fractions of anomalous γ-Ni + Ni$_3$B + Cr$_3$C$_2$ and lamellar Ni–B–Si eutectics are present in the interdendritic regions. Though solidification starts with precipitation of Cr borides, these are extremely fine and low in volume fraction due to insufficient time spent in their solidification range. Cr$_7$C$_3$ and Cr$_{23}$C$_6$ type of carbides precipitate in interdendritic regions and Ni$_3$Si phase is present within γ-Ni dendrites.
- Origin of the microstructure could be understood through Scheil's non-equilibrium solidification simulation which predicted the formation of γ-Ni + Ni$_3$B + Cr$_3$C$_2$ eutectics as a result of the absence of Cr borides due to rapid cooling in the initial stages.
- The unique morphology, high volume fraction, and distribution of eutectic constituents resulted in enhanced hardness of the laser rapid manufactured bushes.

CONFLICT OF INTEREST

On behalf of all authors, the corresponding author states that there is no conflict of interest.

REFERENCES

1. A.K. Bhaduri, R. Indira, S.K. Albert, B.P.C. Rao, S.C. Jain, and S. Ashok Kumar: *J. Nucl. Mater.*, 2004, vol. 334, pp. 109–14. https://doi.org/10.1016/j.jnucmat.2004.05.005.
2. S. Balaguru and M. Gupta: *J. Mater. Res. Technol.*, 2021, vol. 10, pp. 1210–42. https://doi.org/10.1016/j.jmrt.2020.12.026.
3. ASM International: *ASM Metals Handbook*, vol. 6, 9th ed., ASM International, Materials Park, OH, USA, 1993, pp. 794–95.
4. M. Corchia, P. Delogu, F. Nenci, A. Belmondo, S. Corcoruto, and W. Stabielli: *Wear*, 1987, vol. 119, pp. 137–52. https://doi.org/10.1016/0043-1648(87)90105-0.
5. T. Liyanage, G. Fisher, and A.P. Gerlich: *Surf. Coat. Technol.*, 2010, vol. 205, pp. 759–65. https://doi.org/10.1016/j.surfcoat.2010.07.095.
6. R. Kaul, P. Ganesh, S.K. Albert, A. Jaiswal, N.P. Lalla, A. Gupta, C.P. Paul, and A.K. Nath: *Surf. Eng.*, 2003, vol. 19, pp. 269–73. https://doi.org/10.1179/026708403322499182.
7. Q. Ming, L.C. Lim, and Z.D. Chen: *Surf. Coat. Technol.*, 1998, vol. 106, pp. 183–92. https://doi.org/10.1016/S0257-8972(98)00525-8.
8. S. Gnanasekaran, G. Padmanaban, V. Balasubramanian, H. Kumar, and S.K. Albert: *High Temp. Mater. Process.*, 2019, vol. 38, pp. 16–29. https://doi.org/10.1515/htmp-2017-0176.
9. I. Hemmati, V. Ocelík, K. Csach, and J.T.M. De Hosson: *Metall. Mater. Trans. A*, 2014, vol. 45A, pp. 878–92. https://doi.org/10.1007/s11661-013-2004-4.
10. G. Xu, M. Kutsuna, Z. Liu, and H. Zhang: *Mater. Sci. Eng. A*, 2006, vol. 417, pp. 63–72. https://doi.org/10.1016/j.msea.2005.08.192.
11. R. González, M.A. García, I. Penuelas, M. Cadenas, M. del Rocío Fernández, A.H. Battez, and D. Felgueroso: *Wear*, 2007, vol. 263, pp. 619–24. https://doi.org/10.1016/j.wear.2007.01.094.
12. Q. Li, D. Zhang, T. Lei, C. Chen, and W. Chen: *Surf. Coat. Technol.*, 2001, vol. 137, pp. 122–35. https://doi.org/10.1016/S0257-8972(00)00732-5.
13. L.J. da Silva, C.J. Scheuer, and A.S.C.M. D'Oliveira: *Wear*, 2019, vol. 428–29, pp. 387–94. https://doi.org/10.1016/j.wear.2019.04.005.
14. I. Hemmati, J.C. Rao, V. Ocelík, and J.T.M. De Hosson: *Microsc. Microanal.*, 2013, vol. 19, pp. 120–31. https://doi.org/10.1017/S1431927612013839.
15. K.F. Tam, F.T. Cheng, and H.C. Man: *Surf. Coat. Technol.*, 2002, vol. 149, pp. 36–44. https://doi.org/10.1016/S0257-8972(01)01414-1.
16. I. Hemmati, V. Ocelík, and J.T.M. De Hosson: *Phys. Procedia*, 2013, vol. 41, pp. 302–11. https://doi.org/10.1016/j.phpro.2013.03.082.
17. J.C. Pereira, M.C. Taboada, A. Niklas, E. Rayón, and J. Rocchi: *J. Manuf. Mater. Process.*, 2023, vol. 7, pp. 110–30. https://doi.org/10.3390/jmmp7030110.
18. H.J. Kim and Y.J. Kim: *Surf. Eng.*, 1999, vol. 15, pp. 495–501. https://doi.org/10.1179/026708499101516911.
19. S. Lebaili, M. Durand-Charre, and S. Hamar-Thibault: *J. Mater. Sci.*, 1988, vol. 23, pp. 3603–11. https://doi.org/10.1007/BF00540502.
20. G. Chakraborty, R. Rani, R. Ramaseshan, M.A. Davinci, C.R. Das, T. Mathews, and S.K. Albert: *Tribol. Trans.*, 2021, vol. 64, pp. 658–66. https://doi.org/10.1080/10402004.2021.1896059.
21. V. Ramasubbu, G. Chakraborty, S.K. Albert, and A.K. Bhaduri: *Mater. Sci. Technol.*, 2009, vol. 27, pp. 573–80. https://doi.org/10.1179/026708309X12526555493431.
22. C.R. Das, S.K. Albert, A.K. Bhaduri, and R. Nithya: *Mater. Sci. Technol.*, 2007, vol. 23, pp. 771–79. https://doi.org/10.1179/174328407X185802.
23. G. Chakraborty, N. Kumar, C.R. Das, S.K. Albert, A.K. Bhaduri, S. Dash, and A.K. Tyagi: *Surf. Coat. Technol.*, 2014, vol. 244, pp. 180–88. https://doi.org/10.1016/j.surfcoat.2014.02.013.
24. P.R. Reinaldo and A.S.C.M. D'Oliveira: *J. Mater. Eng. Perform.*, 2013, vol. 22, pp. 590–97. https://doi.org/10.1007/s11665-012-0271-7.
25. C. Sudha, P. Shankar, R.V. Subba Rao, R. Thirumurugesan, M. Vijayalakshmi, and B. Raj: *Surf. Coat. Technol.*, 2008, vol. 202, pp. 2103–12. https://doi.org/10.1016/j.surfcoat.2007.08.063.
26. G. Chakraborty, S.K. Albert, and A.K. Bhaduri: *Mater. Sci. Technol.*, 2012, vol. 28, pp. 454–59. https://doi.org/10.1179/1743284711Y.0000000082.
27. L.J. da Silva and A.S.C.M. D'Oliveira: *Wear*, 2016, vol. 350–51, pp. 130–40. https://doi.org/10.1016/j.wear.2016.01.015.
28. S. Balaguru, V. Murali, P. Chellapandi, and M. Gupta: *Nucl. Eng. Technol.*, 2020, vol. 52, pp. 589–96. https://doi.org/10.1016/j.net.2019.08.011.

29. C.R. Das, S.K. Albert, A.K. Bhaduri, and G. Kempulraj: *J. Mater. Process. Technol.*, 2003, vol. 141, pp. 60–66. https://doi.org/10.1016/S0924-0136(02)01130-5.
30. C.P. Paul, A. Jain, P. Ganesh, J. Negi, and A.K. Nath: *Opt. Lasers Eng.*, 2006, vol. 44, pp. 1096–1109. https://doi.org/10.1016/j.optlaseng.2005.08.005.
31. ICDD database, https://www.icdd.com. Accessed 2 June 2022.
32. S. Ômori, Y. Hashimoto, S. Nakamura, K. Hidaka, and Y. Kohira: *J. Jpn. Soc. Powder Metall.*, 1971, vol. 18, pp. 132–35. https://doi.org/10.2497/jjspm.18.132.
33. K.L. Fraga-Chávez, M.J. Castro-Román, M. Herrera-Trejo, L.E. Ramírez-Vidaurri, and I. Aguilera-Luna: *Metals*, 2017, vol. 7, pp. 187–202. https://doi.org/10.3390/met7060187.
34. T.A.M. Haemers, D.G. Rickerby, F. Lanza, F. Geiger, and E.J. Mittemeijer: *J. Mater. Sci.*, 2000, vol. 35, pp. 5691–98. https://doi.org/10.1023/A:1004858508274.
35. J. Ajao and S. Hamar Thibault: *J. Mater. Sci.*, 1988, vol. 23, pp. 1112–25. https://doi.org/10.1007/BF01154022.
36. L.Y. Chen, T. Xu, H. Wang, P. Sang, S. Lu, Z.X. Wang, S. Chen, and L.C. Zhang: *Surf. Coat. Technol.*, 2019, vol. 358, pp. 467–80. https://doi.org/10.1016/j.surfcoat.2018.11.019.
37. A. Prince: *Alloy Phase Equilibria*, Elsevier Publications, New York, 1966, pp. 173–98.
38. L.Y. Chen, H. Wang, C. Zhao, S. Lu, Z.X. Wang, J. Sha, S. Chen, and L.C. Zhang: *Surf. Coat. Technol.*, 2019, vol. 369, pp. 31–43. https://doi.org/10.1016/j.surfcoat.2019.04.052.
39. E.E. Kornienko, A.A. Nikulina, A.G. Bannov, and A.S. Ivashutenko: *Met. Sci. Heat Treat.*, 2022, vol. 63, pp. 637–43. https://doi.org/10.1007/s11041-022-00742-9.